**Showcasing research from an international collaboration conducted at the Deutsches Elektronen-Synchrotron DESY, Hamburg, Germany.**

Ultrafast dynamics of fluorene initiated by highly intense laser fields

We present an investigation of the ultrafast dynamics of the polycyclic aromatic hydrocarbon fluorene initiated by an intense femtosecond near-infrared laser pulse (810 nm) and probed by a weak visible pulse (405 nm). Using a multichannel detection scheme (mass spectra, electron and ion velocity-map imaging), we provide a full disentanglement of the complex dynamics of the vibronically excited parent molecule, its excited ionic states, and fragments.

As featured in:
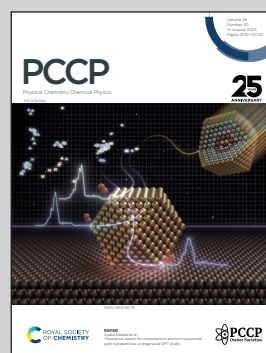
See Melanie Schnell *et al.*,
Phys. Chem. Chem. Phys.,
2024, **26**, 20261.

ROYAL SOCIETY
OF CHEMISTRY

rsc.li/pccp

PCCP
Owner Societies

Ultrafast dynamics of fluorene initiated by highly intense laser fields†

Diksha Garg, [ab] Pragya Chopra, [ac] Jason W. L. Lee, [ad] Denis S. Tikhonov, [a] Sonu Kumar, [ab] Oender Akcaalan, [a] Felix Allum, ‡§[d] Rebecca Boll, [e] Alexander A. Butler, [d] Benjamin Erk, [a] Eva Gougoula, [a] Sébastien P. Gruet, [a] Lanhai He, [f] David Heathcote, [d] Ellen Jones, [d] Mehdi M. Kazemi, [a] Jan Lahl, [g] Alexander K. Lemmens, [hi] Zhihao Liu, [d] Donatella Loru, [a] Sylvain Maclot, [j] Robert Mason, [d] James Merrick, [d] Erland Müller, [a] Terry Mullins, [fe] Christina C. Papadopoulou, [a] Christopher Passow, [a] Jasper Peschel, [g] Marius Plach, [g] Daniel Ramm, [a] Patrick Robertson, ¶[d] Dimitrios Rompotis, [ae] Alcides Simao, ‖[a] Amanda L. Steber, **[a] Ayhan Tajalli, [a] Atia Tul-Noor, [a] Nidin Vadassery, [fk] Ivo S. Vinklárek, [f] Simone Techert, [a] Jochen Küpper, [fblk] Anouk M. Rijs, [m] Daniel Rolles, [n] Mark Brouard, [d] Sadia Bari, [ao] Per Eng-Johnsson, [g] Claire Vallance, [d] Michael Burt, [d] Bastian Manschwetus ††[a] and Melanie Schnell *[ac]

We present an investigation of the ultrafast dynamics of the polycyclic aromatic hydrocarbon fluorene initiated by an intense femtosecond near-infrared laser pulse (810 nm) and probed by a weak visible pulse (405 nm). Using a multichannel detection scheme (mass spectra, electron and ion velocity-map imaging), we provide a full disentanglement of the complex dynamics of the vibronically excited parent molecule, its excited ionic states, and fragments. We observed various channels resulting from the strong-field ionization regime. In particular, we observed the formation of the unstable tetracation of fluorene, above-threshold ionization features in the photoelectron spectra, and evidence of ubiquitous secondary fragmentation. We produced a global fit of all observed time-dependent photoelectron and photoion channels. This global fit includes four parent ions extracted from the mass spectra, 15 kinetic-energy-resolved ionic fragments extracted from ion velocity map imaging, and five photoelectron channels obtained from electron velocity map imaging. The fit allowed for the extraction of 60 lifetimes of various metastable photoinduced intermediates.

[a] *Deutsches Elektronen-Synchrotron DESY, Hamburg, Germany. E-mail: melanie.schnell@desy.de*

[b] *Department of Physics, Universität Hamburg, Hamburg, Germany*

[c] *Institute of Physical Chemistry, Christian-Albrechts-Universität zu Kiel, Kiel, Germany*

[d] *Chemistry Research Laboratory, Department of Chemistry, University of Oxford, Oxford, UK*

[e] *European XFEL, Schenefeld, Germany*

[f] *Center for Free-Electron Laser Science CFEL, Deutsches Elektronen-Synchrotron DESY, Germany*

[g] *Department of Physics, Lund University, Lund, Sweden*

[h] *Van't Hoff Institute for Molecular Sciences, University of Amsterdam, Amsterdam, The Netherlands*

[i] *FELIX Laboratory, Radboud University, Nijmegen, The Netherlands*

[j] *Université Claude Bernard Lyon 1, Villeurbanne, France*

[k] *Department of Chemistry, Universität Hamburg, Hamburg, Germany*

[l] *Center for Ultrafast Imaging, Universität Hamburg, Hamburg, Germany*

[m] *Division of BioAnalytical Chemistry, Vrije Universiteit Amsterdam, Amsterdam, The Netherlands*

[n] *J. R. Macdonald Laboratory, Department of Physics, Kansas State University, Manhattan, KS, USA*

[o] *Zernike Institute for Advanced Materials, University of Groningen, Groningen, The Netherlands*

This journal is © the Owner Societies 2024

Phys. Chem. Chem. Phys., 2024, **26**, 20261–20272 | **20261**

1 Introduction

Polycyclic aromatic hydrocarbons (PAHs) are a large class of molecules that consist of carbon and hydrogen atoms. Each PAH contains at least two rings, of which at least one is aromatic. These molecules play an important role in astrochemistry since they are estimated to account for about 10% of all galactic carbon.[1,2] PAHs can also form in combustion reactions of fossil fuels, which lead to the presence of PAHs in the Earth's atmosphere. Here, they act as environmental pollutants, and they impact the health of the population.[3,4] In the interstellar medium (ISM) and planetary atmospheres, PAHs are subjected to high-energy particles.[5–8] Therefore, investigating PAHs' radiation and photoinduced chemistry is a compelling study with broad implications. Upon passing near the molecule, fast-charged particles, such as electrons or alpha particles, will create a short, strong electric field comparable to the atomic scales. To mimic such strong-field excitation of molecules, we can apply strong-field laser pulses in the laboratory environment.

Previously, strong-field-induced ionization and fragmentation of PAHs were studied with table-top laser setups.[9–12] In particular, laser pulses with peak intensities of about $\sim 10^{14}$ W cm^{-2} interacting with PAHs have produced ionic species up to tetracations.[9] Investigations of the ultrafast ionization and fragmentation of PAHs induced by highly energetic XUV photons have recently gained attention in the scientific community for tracing down mechanisms of photochemical reactions. The ultrafast pump–probe studies with ultrashort XUV pulses produced either by high-harmonic generation (HHG) sources[13–16] or free-electron lasers (FELs)[17–19] revealed rich dynamics of charge state evolutions up to PAH trications. Femtosecond strong-field laser pulses, produced by Ti:Sa lasers, were also used to induce dynamics in benzene and toluene.[20,21] These studies found interesting dynamics, such as oscillations between vibrational states in toluene,[21] or conical intersection relaxation[20] in Jahn–Teller benzene cations.[22,23]

In this work, we present an investigation of the dynamics of a three-ring PAH fluorene ($C_{13}H_{10}$, FLU, see Fig. 1). This molecule can be thought of as a three-ring analog of indene, the first pure PAH identified in the ISM.[24,25] The XUV-induced dynamics of FLU have recently been studied in detail.[17,19] As a follow-up, here we chose to investigate how the observed dynamics change in a different excitation regime. We used ultrashort strong-field infrared (IR) laser pulses to excite FLU and subsequently probed it using a weaker visible (VIS) pulse. The pump pulse peak intensity was estimated to be

3.3×10^{13} W cm^{-2}, which corresponds to a Keldysh parameter value of $\gamma = 1.4$,[26] for the single ionization of FLU. Based on the calculated γ value and considering a non-uniform spatial distribution of intensities in the laser pulse, we expect to observe a mixed regime of strong-field ionization that could show features of both tunneling ionization (TI, $\gamma \ll 1$) and multiphoton ionization (MPI, $\gamma \gg 1$). The interaction of the strong-field laser with FLU results in the production of electrons and multiple ions, which were measured using a double-sided velocity map imaging (VMI) spectrometer. VMI enabled the disentangling of the various photodissociation fragmentation pathways on the basis of momentum. In addition, the time-of-flight (TOF) mass spectra (MS) of the ions were measured. This multi-channel data accumulation allowed for a detailed and comprehensive decomposition of the strong-field-induced dynamics of FLU. In this manuscript, we describe the experimental details, data analysis, and theoretical calculations. This is followed by pump–probe independent results, dynamical observations, and conclusions.

2 Methods

2.1 Experimental details

The IR (810 nm)–VIS (405 nm) pump–probe experiments were carried out at the permanent CAMP end-station[27] at beamline BL1 at the free-electron laser in Hamburg (FLASH)[28] facility. A Ti:Sa laser system[29] produced pulses at 810 nm. The pulses were then split into two components with a beamsplitter in a ratio of 75 : 25.[30] Most of each pulse was used as an IR pump, and a part of each pulse went to the second harmonic generation (SHG) to produce a weaker VIS probe pulse of 405 nm. The duration (full width at half maximum, FWHM) of the IR pulse was 60 fs, while the duration of the VIS pulse was estimated to be less than 150 fs. We measured the ion yield produced as a function of pump–probe delay time. The arrival time of the probe pulse was varied from −1 ps to +1 ps in 15 fs steps relative to the pump pulse using a mechanical delay stage.

The CAMP end-station houses a double-sided ion and electron VMI spectrometer,[31,32] enabling the measurement of ion and electron kinetic energies simultaneously. An open port in the vacuum chamber at the CAMP end-station allowed for the installation of a source chamber equipped with a high-temperature Even-Lavie valve (ELV),[33] two subsequent skimmers and a differential pumping step for sample introduction into the experiment.

The sample of FLU was purchased from Sigma-Aldrich and Thermo Fisher with 98% purity and used without further purification in two different beamtimes performed in 2018 (F-20170540) and 2023 (F-20211752), respectively. In the experiment, fluorene powder was heated to 200 °C in an in-vacuum reservoir, implemented in the ELV, in order to obtain sufficient vapor pressure. The gas-phase molecules were then introduced into the vacuum chamber by means of a helium carrier gas with a backing pressure of 1 bar. A pulsed molecular jet was doubly skimmed on the way to the interaction region to obtain a well-collimated molecular beam.
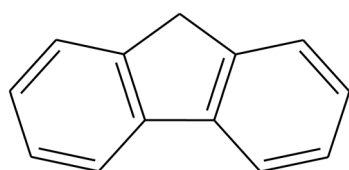

Fig. 1 Molecular structure of fluorene (FLU), molecular formula $C_{13}H_{10}$.

20262 | Phys. Chem. Chem. Phys., 2024, 26, 20261–20272

This journal is © the Owner Societies 2024

Three types of data obtained from the experiments have been used for the analysis, namely, the TOF-MS, the electron VMI, and the ion VMI. Each ion and electron dataset were acquired using a combination of microchannel plate (MCP) in chevron configuration and phosphor screens, P47 and P20, respectively. The TOF-MS were obtained directly from the MCP readout with the help of a 2 GHz analog-to-digital-converter (ADQ412AC-4G-MTCA). The velocity map images of all individual ionic species simultaneously, together with lower-resolution TOF-MS, were obtained using a Pixel Imaging Mass Spectrometry (PImMS2) sensor.[34,35] Lastly, the electron data was obtained directly from a charge-coupled device (CCD, in 2018) or complementary metal–oxide–semiconductor (CMOS, in 2023) camera readout.

2.2 Data analysis

Data extraction and analysis were performed using home-written scripts. To retrieve and analyze the data from the TOF-MS and electron VMI data, a combination of the BeamtimeDAQAccess[36] and CAMPFancyAnalysis[37] Python libraries was used. For the analysis of the PImMS data, a home-written set of LabView scripts and the CAMPFancyAnalysis library were employed. The inverse Abel transformation for the ion images was performed using the onion peeling method,[38] processing of the photoelectron angularly-integrated images was done using direct Abel transformation. Both routines were used as implemented in the PyAbel package.[39,40]

A detailed description of the recoil-frame covariance analysis for the ion VMI data can be found elsewhere.[17,41–45] The photoelectron–photoion covariance analysis (PEPICOV) was performed in the following way:[46,47] first, each single-shot electron image was converted into the radial distribution function (RDF), and each single-shot TOF-MS was converted into the mass-over-charge (m/z) MS. The centers of the images and the momentum calibration were determined based on the helium II photoelectron data, which was obtained in pre- and post-measurements for the same molecular beam with 41 eV XUV radiation from FLASH, published in ref. 17,19. Then, the covariance map was obtained as

$$\text{cov(IY, PEY)} = \langle \text{IY·PEY} \rangle - \langle \text{IY} \rangle \cdot \langle \text{PEY} \rangle,$$

where "IY" denotes ion yield at a given m/z value, "PEY" denotes photoelectron yield at a given image radius value, and $\langle \ldots \rangle$ denotes averaging over all shots. A partial covariance correction for fluctuations in the pressure in the chamber was also applied.[48] Then, along the image radius axis of the map, a direct Abel inversion transformation was performed.

The observed dependencies of the ion and electron yields as a function of pump–probe delay time were fit as linear combinations of basis functions, describing pump–probe dynamical response[17,49,50] using the MC^{3}Fitting software.[51] First, a global fitting was done, followed by the Monte-Carlo sampling of the parameters' uncertainties, as described in detail in ref. 50. A simultaneous fitting was performed for the multiple channel data for the parent ions (from the high-resolution TOF-MS), momentum-disentangled fragment ion yields (from the ion

VMI), and photoelectron yields (from the electron VMI). Fitting was done for 40 datasets of ion yield *versus* pump–probe delay time, which comprise momentum-resolved fragment ion yields of ions having 5 to 12 carbon atoms, the parent monocation, dication, and trication, dehydrogenated parent monocation, momentum-resolved dications of fragment ions having 5, 7, and 11 carbon atoms, and electron yields corresponding to five photoelectron bands. Fitting multiple datasets together enabled an estimation of the overlapping time of the pump and probe pulses (t_0). Using this t_0, four momentum-resolved fragment ions (1 to 4 carbon atoms) with more than one transient feature were also fitted, giving out 12 datasets.

The detailed results of the data analysis are given in the ESI.†

2.3 Computational details

To calculate the MS of FLU, augmented Born–Oppenheimer molecular dynamics (aBOMD) simulations of the fragmentation of FLU were done using the DissMD script from the PyRAMD software.[52] The algorithm was based on the QCEIMS idea,[53,54] and the modifications are described in detail in ref. 18,55. The forces for aBOMD were computed with the xTB software[56] at the semi-empirical GFN2-xTB level of theory[57] that was shown to be suitable for the fragmentation pattern predictions.[58] To emulate the high-energy excitation regime, the excitation energy was represented as $n \times h\nu$, where n is the number of photons, and $h\nu$ is the photon energy, which was taken to be 1.5 eV (corresponding to a wavelength of 810 nm). The parameter n was sampled from the Poisson distribution with a mean number of photons $\langle n \rangle = 40$, and the result was adjusted to fit in the interval of $6 \leq n \leq 100$ by setting the outlier n value to the closest value of $n = 6$ or $n = 100$.

The energetics of the reaction $C_2^{2+} \rightarrow 2C^+$, discussed later in Section 3.2.5, were computed at CCSD(T)/aug-cc-pVTZ[59–61] using the ORCA 5 software.[62] The geometries of C_2^{2+} were optimized for the singlet, triplet, and quintet multiplicities, with the triplet being the lowest energy state. For the carbon monocation, doublet and quadruplet states were computed, with the doublet found to be the lowest in energy. All the geometries and energies are given in the ESI.†

3 Results and discussion

3.1 Roadmap of the analysis

In the following two sections, we will present the analysis of the strong-field-induced reaction dynamics of FLU. First, we will discuss the main time-independent features observed in the photoion and photoelectron signals without consideration of the pump–probe effects. There, we will focus on the individual spectra of the species and on the covariance techniques that allow us to find relations between the different observables. Afterward, we will look into the pump–probe dependencies of the discussed signal, extracting the information on the ultrafast photochemical processes in FLU.

This journal is © the Owner Societies 2024

Phys. Chem. Chem. Phys., 2024, **26**, 20261–20272 | **20263**

3.2 Time-independent observations

3.2.1 Mass spectra. The behavior of benzene, benzene derivatives,[20,21,63,64] and PAHs[9–12] in strong laser fields has been investigated for decades. The general fragmentation patterns of PAHs are very similar: at lower peak field intensities ($\sim 10^{13}$ W cm^{-2}),[9] only single ionization is visible in the MS. As the peak power is increased, a rise of the parent monocation formation as well as the formation of the parent dication and monocationic and dicationic fragments are observed. At high peak powers ($\sim 10^{14}$ W cm^{-2}), trications and even tetracations occur in the MS for PAHs.[9,64]

In the first set of experiments, in which FLU was subjected to IR pulses of variable intensity, we also observed this ubiquitous behavior, which can be seen in Fig. 2. We see the production of the highly-charged parent species up to the trication (FLU^{3+}), as well as a subsequent rise in the production of the fragment ions upon increasing the IR pulse peak power. The production of various fragments varies depending on the species. For instance, the parent monocationic species (FLU$^+$), such as $C_{13}H_{10}^+$ and $C_{13}H_{10}^{2+}$, monotonously increase with the rise of the IR pulse peak power. However, the highly-charged species, such as the parent trication (FLU^{3+}), appear only as a threshold power of about 4×10^{13} W cm^{-2} is reached (see ESI† for details). This suggests that there might be an interplay of MPI and TI strong-field ionization regimes, as discussed in the literature.[64–67]

3.2.2 Photoelectron spectra. The photoelectron spectrum (PES) of FLU averaged over all pump–probe delays (~ 2 ps in total) is shown in Fig. 3. The experimental results clearly show above threshold ionization (ATI) features as distinct peaks with equal spacing corresponding to the photon energy of the IR pulse (1.5 eV).[68] The ATI peaks were fitted using the expression

$$E_k = (n_{\min} + k)h\nu - \text{IP} - U_p, \qquad (1)$$
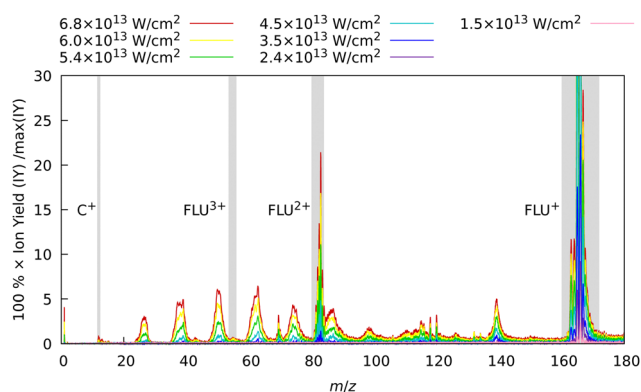
Fig. 2 Experimental MS of FLU obtained with only the IR laser pulse for different intensities. The spectra were background-subtracted and normalized to the maximum intensity peak of the FLU monocation ($C_{13}H_{10}^+$, m/z = 166) observed with the unattenuated data corresponding to a laser peak intensity of 6.8×10^{13} W cm^{-2}. Gray-shaded areas highlight the four peaks of interest: C$^+$ (m/z = 12), FLU^{3+} (m/z = 55.3), FLU^{2+} (m/z = 83), and FLU$^+$ (m/z = 166). The full-range spectrum in the logarithmic scale and signal dependencies of the intensities of these peaks as a function of laser intensities are given in the ESI.†
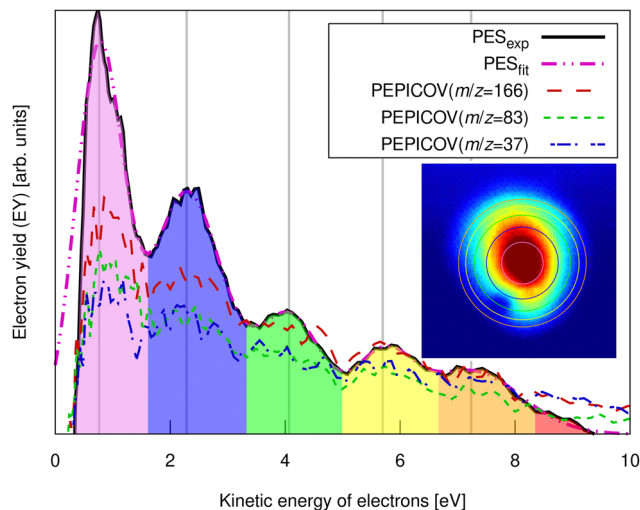
Fig. 3 Experimental pump–probe delay averaged photoelectron spectrum of FLU (solid line) and PEPICOV-disentangled spectra for the parent FLU$^+$ (m/z = 166), FLU^{2+} (m/z = 83), and the fragment ion at m/z = 37. The different colored areas underneath the spectrum and the vertical lines highlight different ATI peak orders. The inset shows the distorted raw electron VMI image. The vertical lines correspond to the circles in the inset image. The full PEPICOV map is available in the ESI.†

where E_k is the position of the k-th ATI peak (k = 1, 2, 3, 4, 5), $n_{\min}$ = 6 is the minimal number of IR photons with energy $h\nu$ = 1.5 eV to produce ionization of FLU, IP = 7.9 eV is the ionization potential of FLU, and U_p is the fitted pondermotive energy,[69–71] which was found to be U_p = 2.0 eV. Based on this value, we estimated the peak intensity of the laser pulses to be 3×10^{13} W cm^{-2}, which agrees with the estimated value from the laser parameters. Details of the fitting procedure and laser parameter estimations are provided in the ESI.†

The ATI features are clear signatures of MPI processes. The photoelectron–photoion covariance (PEPICOV) analysis revealed that the disentangled PES corresponding to all the ionic fragments look very similar and resemble the PES of the whole system, with the same set of ATI peaks (see dashed PEPICOV lines in Fig. 3). This indicates that the MPI regime dominates TI in producing low-charge parent ions and fragments. The similarity of the PEPICOV features for the FLU monocation (m/z = 166) and dication (m/z = 83) probably points to the photoionization proceeding sequentially, *i.e.*, first, monocations are produced as FLU + IR → FLU$^+$ + e$_1^-$, where e$_1^-$ is the photoelectron appearing from the first ionization step. Then, the double ionization occurs according to a reaction FLU$^+$ + IR → FLU^{2+} + e$_2^-$, where e$_2^-$ is the second ejected electron, which should have a different ATI spectrum. The amount of the monocations in the MS is 4–5 times higher than of the dications, which means that mainly the covariance of FLU^{2+} with e$_1^-$ will be visible, as the number of e$_1^-$ will be exceedingly larger than of e$_2^-$. Additionally, the general mechanism of fragmentation implies obtaining first a highly excited mono- or dicationic state of the parent, which later decays into the charged fragments, thereby providing similar PES.

3.2.3 Recoil-frame covariance. Recoil-frame covariance analysis was performed on the mass-resolved VMI data to

20264 | *Phys. Chem. Chem. Phys.*, 2024, **26**, 20261–20272

This journal is © the Owner Societies 2024

distinguish the various measured fragmentation channels. This approach was shown to be very effective in disentangling the fragmentation pathways of complex PAH molecules.[17–19] In brief, this method correlates the relative positions of two ions (the reference ion and the ion of interest) on the imaging detector. If the ion of interest is produced simultaneously with the reference ion, we see a recoil feature, a positive covariance in the opposite direction to that defined by the reference ion, which we choose to be upwards. More information on this technique can be found in ref. 41.

When we look at the covariance images obtained from the strong-field excitation (Fig. 4), we see a major difference from the results observed upon the ionization and fragmentation induced with the single-photon XUV.[17,19] In the case of XUV excitation-ionization, the recoil features appeared on the diagonals, corresponding to C_2H_x-fragment loss (shown as dashed boxes in Fig. 4). However, in the strong-field regime, we see distinct features off these diagonals, *e.g.*, the $C_3H_x^+$ ion of interest recoiling against $C_7H_y^+$, or $C_4H_x^+$ against $C_6H_y^+$. Such off-diagonal signals indicate odd-carbon loss fragmentation channels, which were not observed in the XUV regime. The most probable reason for such a fragmentation pattern is that a larger variety of final states can be reached in the strong-field multiphoton regime compared to a single-photon excitation due to a change in selection rules.

We also see recoil relations between the smallest fragments: $C_3H_x^+$ ion of interest against $C_2H_y^+$. A significant broadening of the recoil feature (see enlarged insets in Fig. 4) may indicate that they are not produced in the same dissociation event but sequentially. In this case, the additional fragments would carry

additional momentum, blurring out the recoil feature of the correlated ions.

A significant asymmetry in the intensities of the observed covariances was noted. On the one hand, in Fig. 4, we see clear signals for the small reference ions (C_2^+–C_5^+) of interest recoiling against larger monocations (C_8^+–C_{11}^+) in the pairwise dissociation of the parent and of the acetylene-loss fragment $C_{11}H_8^{2+}$. On the other hand, the inverted covariances, *e.g.*, $C_{10}H_y^+$ ion of interest against $C_3H_x^+$, are significantly less intense (however, present). This asymmetry is also a signature of sequential fragmentation, in which the fraction of events producing stable large fragments is much lower than the fraction of metastable large fragments that undergo further fragmentation, producing smaller ions without larger counterparts.

3.2.4 Formation and fragmentation of tetracation. While the trication FLU^{3+} is clearly visible in the MS data (Fig. 2), we have not observed any traces of the intact FLU tetracation (FLU^{4+}) in the MS data. However, we see evidence of the parent tetracation fragmentation in the ion VMI of dicationic fragments, namely $C_7H_x^{2+}$ and $C_{11}H_x^{2+}$ recoiled from a doubly-charged counterion. In Fig. 5, the pump–probe delay averaged VMI image for the $C_7H_x^{2+}$ ion and the corresponding angularly-integrated ion momentum distribution are shown. In the VMI image, three features are observed: a near-the-center signal, a larger circle, and a halo. Large fragments, such as $C_7H_x^{2+}$ and $C_{11}H_x^{2+}$, are mostly produced from the parent ion as a result of the reaction

$$C_{13}H_{10}^{(n+m)+} \rightarrow C_7H_x^{n+} + C_6H_y^{m+} \tag{2}$$
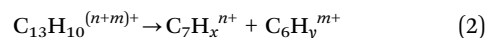
which we will denote as (n,m) channel. Upon the increase of the fragments' charges (n and m), the Coulomb repulsion also increases as a product of these charges ($n \times m$). This increasing repulsion increases the kinetic energy release (KER), which leads to an increase in the momentum of individual fragments. Therefore, we can attribute three observed features to three fragmentation channels: (2,0), (2,1), and (2,2).
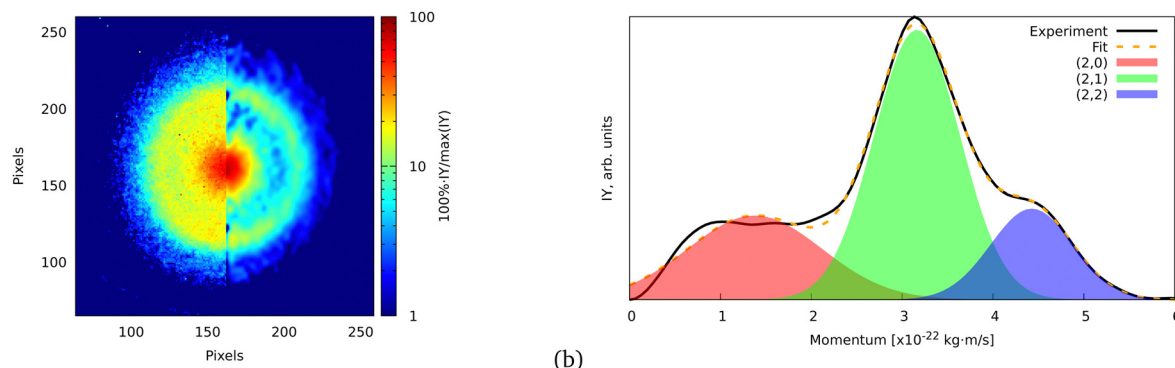
The momentum value of $C_7H_x^{2+}$ formed *via* dissociation of FLU^{4+} into the (2,2) channel is calculated to be $\sim 4.6 \times 10^{-22}$ kg m s^{-1} using the experimental KER value of FLU^{2+} dissociation for the (1,1) channel (2.46 ± 0.04 eV),[18] which is in agreement with the observed momentum value of $(4.43 \pm 0.02) \times 10^{-22}$ kg m s^{-1} (calculation is provided in the ESI†). This value is obtained by fitting the momentum profile of $C_7H_x^{2+}$ as shown in Fig. 5. The (2,2) channel is a direct indication of the FLU^{4+} production. However, FLU^{4+} itself is not observed in the MS, which indicates that it is unstable.

3.2.5 Feature at $m/z = 12$. A distinctive feature appears in the strong-field induced mass spectra of substituted benzenes[20,21,63,64] and PAHs,[9–12] that is not observed in analogous XUV-induced mass spectra.[17,19] This feature is a set of peaks at $12 \leq m/z \leq 16$ with the main signal appearing at $m/z = 12$. This peak can either correspond to C^+ or to C_2^{2+} (see Fig. 2 and 6). On the one hand, if this fragment is mainly C_2^{2+}, this would strongly indicate a preferred acetylene loss mechanism for PAH fragmentation, *i.e.*, the PAH backbone breaks up into smaller chunks by losing $C_2H_x^{q+}$ ($q = 0,1,2$) fragments. Such preference was observed in the
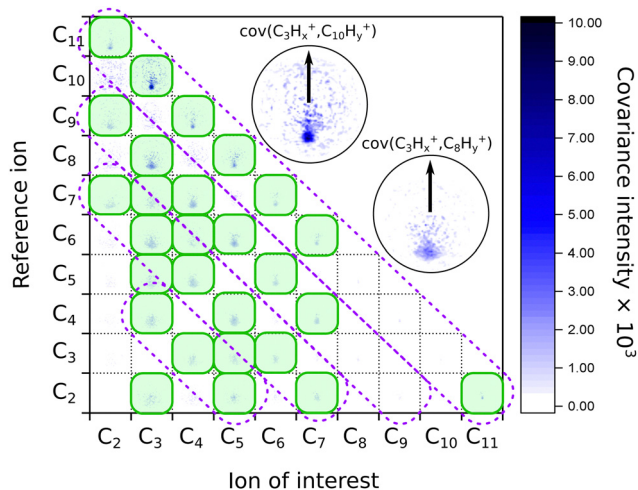
Fig. 4 Matrix of the recoil-frame covariance images for different pairs of recoiling ions obtained from averaging all pump–probe delays of the IR-VIS pump–probe experiment. The diagonal violet dashed boxes indicate where the signal was present in the case of the XUV-UV experiment on FLU, from ref. 19. The green shaded boxes show the most intense recoil covariance signals in the current experiment. The two insets show zoomed images of the $C_3H_x^+$ ion of interest recoiling against the $C_{10}H_y^+$ and $C_8H_y^+$ reference ions, respectively. The arrows in both insets show the reference ion direction for all the recoil-frame covariance images. An enlarged version of this map without notations is available in the ESI†.

This journal is © the Owner Societies 2024

Phys. Chem. Chem. Phys., 2024, **26**, 20261–20272 | **20265**

Fig. 5 (a) Ion VMI of the $C_7H_x^{2+}$ fragment from FLU. The left side of the image is the raw experimental data, while the right part is the result of filtering and Abel inversion with the BASEX method. (b) Angularly integrated momentum distribution function of the $C_7H_x^{2+}$ ion with a three-Gaussian profile fit. The fit was performed similarly to the ATI PES, for which details are given in the ESI.† The shaded areas indicate the individual fit components that represent (2,0), (2,1), and (2,2) channels.

XUV-induced fragmentation patterns (Fig. 4), which can be related to the hydrogen abstraction acetylene addition (HACA) mechanism of PAH formation,[72–74] that can be important due to the presence of the C_2 molecule[75] in space, for instance in comets.[76] On the other hand, if the m/z = 12 peak corresponds to C^+, that could indicate a high-energy stochastic fragmentation of the backbone.

We do not observe any conclusive recoil-frame covariance features for this fragment. However, this might also be due to it displaying the strongest distortion of the ion VMI among all fragments, which makes the center determination for this ion complicated. The momentum distribution map for this ion has three dissociation channels that can be interpreted as (1,0), (1,1), and (1,2) or as (2,0), (2,1), and (2,2) (see eqn (2)), which does not favor either of the interpretations. However, the TOF-MS data is more in favor of the C^+ interpretation of this peak: we see two peaks that are positioned at m/z = 12 and m/z = 13 (Fig. 6). This pattern suggests that this feature corresponds to C^+ because, in case of the dication, we would expect m/z = 12 for C_2^{2+}, m/z = 12.5 for C_2H^{2+}, and m/z = 13.0 for $C_2H_2^{2+}$. The isotope ^{13}C in this case does not explain the observed pattern since, in the natural abundance, it is expected to be around 1% of the most intense peak, while the ratio of the peaks at m/z = 12 and m/z = 13 is about 2 : 1, respectively (Fig. 6).

To support this assignment from the mass spectrum, we have calculated the equilibrium dissociation energy (D_e) for the reaction $C_2^{2+} \rightarrow 2C^+$ at the CCSD(T)/aug-cc-pVTZ level of theory. The obtained value of $D_e = -5.3$ eV shows that this reaction is strongly exothermic, which means that C^+ is a more energetically favorable ion. The estimated lifetime of the metastable triplet C_2^{2+} into two C^+ ions is 0.9 ns (see ESI† for details), which makes the detection of this species with MS impossible. Using aBOMD simulations of the fragmentation dynamics, we also observe peaks at the m/z region of interest (12 ≤ m/z ≤ 14), which all correspond to CH_x^+ species (Fig. 6). The further fragmentation of CH_x^+ up to C^+ could not be traced with the semi-empirical method used for aBOMD due to electronic problem convergence issues. Nevertheless, from a combination of experimental data and simulations, we conclude that the
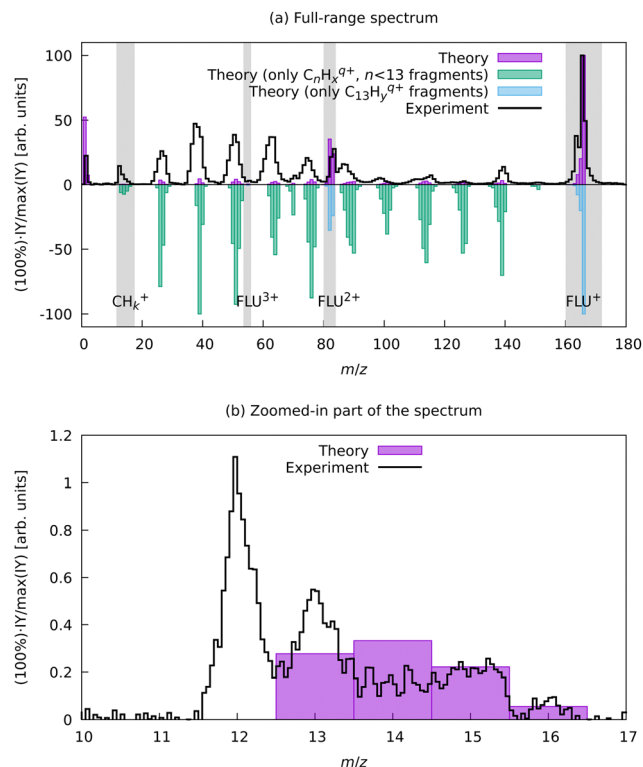
fragments in the range 12 ≤ m/z ≤ 16 in the high laser power-induced MS of FLU correspond to C^+.

3.3 Pump–probe-dependent results

Now, we present the analysis of the time-resolved pump–probe measurements for our system. The pump pulse was a strong-field IR (810 nm) laser pulse with an estimated peak power of 3×10^{13} W cm^{-2}. This pulse initiated the ionization and fragmentation dynamics in FLU, which was described in the previous section. The probe pulse was a weaker VIS pulse (405 nm) produced from the same laser system. The comparison of the pump-only, probe-only, and pump–probe averaged MS is given in the ESI.† We monitor various observables (various ion and electron yields) as a function of the delay between pump and probe pulses (t). We chose the temporal overlap of both pulses (t_0) to be at t = 0. The region in which the probe pulse comes before the pump pulse is $t < 0$, and the region in which the probe comes after the pump is $t > 0$.

The time-dependent changes in the MS, PES, and a typical ion momentum distribution map of the $C_4H_x^+$ ion are shown in Fig. 7. The momentum map illustrates the evolution of the momentum of the ion extracted from the ion VMI (as in Fig. 5b) as a function of pump–probe delay t. In the pump–probe-dependent MS, we see similar trends for the fragmentation dynamics of PAHs as were observed with the XUV-pumped experiments.[17,19] In the $t < 0$ region, we see more of the parent species than in the $t > 0$ region. For the fragments, this trend is inverse: for $t < 0$, we see fewer ions than for $t > 0$. Such behavior indicates that the pump pulse produces an excited state ensemble, and the probe pulse destroys it by pumping even more energy to overcome fragmentation thresholds. This is observed for the PAH in both XUV-excited regimes probed with IR and VIS pulses as well as for benzene and toluene excited by a strong-field laser.[20,21]
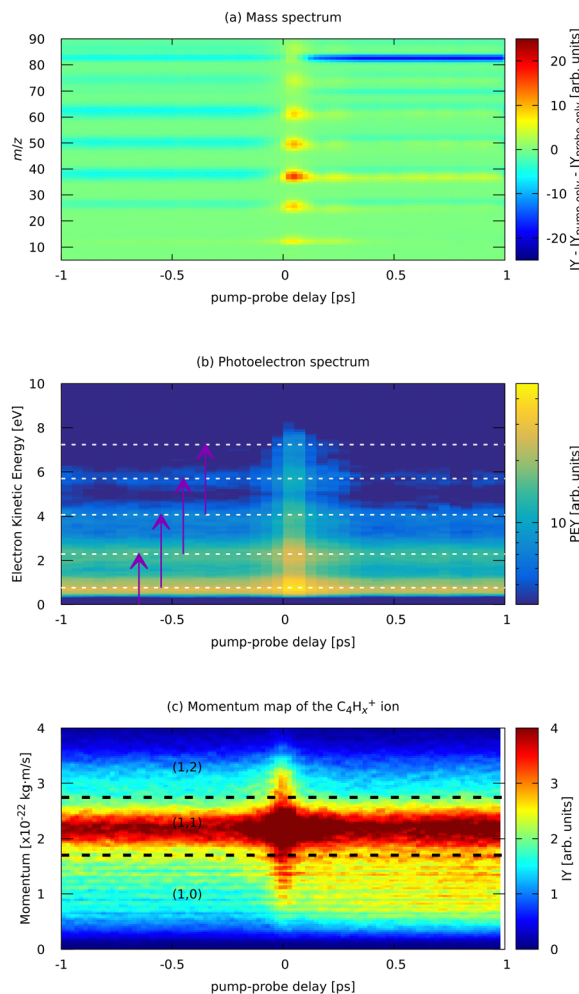
Near the temporal overlap of the two laser pulses (t = 0), there is a strong increase in the ion production of all kinds of ions, as well as an increase in the yields of the ATI peaks. The PES (Fig. 7b) shows qualitatively the same ATI spectrum given by eqn (1) being present in the whole range of the pump–probe

20266 | *Phys. Chem. Chem. Phys.*, 2024, **26**, 20261–20272

This journal is © the Owner Societies 2024

Fig. 6 Experimental and aBOMD-calculated theoretical MS of FLU. The theoretical spectrum was obtained as a distribution of the various fragments obtained from all MD trajectories as a function of the m/z. (a) shows the full m/z-range MS, with the top part giving a comparison of the total MS and the bottom traces showing renormalized contributions of only the parent species with variable degree of dehydrogenation ($C_{13}H_y^{q+}$) and the carbon backbone fragmentation results ($C_nH_y^{q+}$, $n < 13$). (b) shows a zoom for a region between $m/z = 10$ and $m/z = 17$, where in theoretical calculations only the fragments CH_x^+ with $1 \leq x \leq 4$ were observed.

Fig. 7 Experimental parts of the pump (810 nm) – probe (405 nm) dependent MS (a) and photoelectron spectrum (b) of FLU, and (c) ion momentum distribution map of the $C_4H_x^+$ fragment. Horizontal lines in (b) indicate the positions of the ATI peaks from Fig. 3. Purple arrows in (b) indicate the probe photon conversion of the ATI electrons. Horizontal lines in (c) show the approximate delimiters of the (1,0), (1,1), and (1,2) channels of the $C_4H_x^+$ ion. The ion yield (IY) in the MS corresponds to background-subtracted values, i.e., with corresponding values of pump-only and probe-only spectra subtracted. The full m/z-range version of (a) is available in the ESI.†

delays. The new photoelectron features, different from the ATI pattern, do not appear in the PES because the probe photons are just twice the energy of the IR pump photons. The transient increase in each ATI peak's intensity arises from transferring each k-th ATI peak into the $(k + 2)$-th peak by a probe VIS photon with 3 eV of energy (see eqn (1) and vertical arrows in Fig. 7(b) for details). The fitted lifetimes of the transients in the ATI bands seem to decrease with increasing order of the band, going from 102 ± 4 fs to 83 ± 3 fs (Table 1). However, they are all centered around 90 fs, which might indicate that the source of these ATI bands is the same set of excited states of the neutral FLU parent molecule.

Based on the channels observed in XUV-pumped investigations[13−19] and the time-independent results observed in the IR-only case from the previous section, the general scheme for the observed strong-field induced dynamics of FLU in the IR-VIS regime can be described as summarized in Fig. 8. Here, we will briefly describe it. Upon interaction with the IR pump pulse, FLU can produce multiple parent species, from the excited neutral molecules (FLU^0) to tetracations (FLU^{4+}). The probe VIS pulse can ionize the near-threshold species, providing the observed transient increase in the production of the higher-

charge parent ions, which we directly detect from the MS. The excited parent species (FLU^0, FLU^+, FLU^{2+}, FLU^{3+}, and FLU^{4+}) can fragment, producing the fragments in different momentum channels (n,m), i.e., (0,0), (1,0), (1,1), and so forth. The probe photon can increase the fragmentation charge state by one, switching from a (n,m) dissociation channel to a $(n + 1,m)$ channel. The fragments can spontaneously fragment further into smaller species. However, the probe pulse can also enhance this fragmentation in the smaller fragments of the (1,0) channel, leading eventually to the C^+ fragment, for which we see a transient increase in production. All the fitted lifetimes are shown in Fig. 9 and Table 1, and all the fitted pump–probe dependencies of the ion yield and numerical values are given in ESI.†

This journal is © the Owner Societies 2024

Phys. Chem. Chem. Phys., 2024, **26**, 20261–20272 | **20267**

Table 1 Transient lifetimes observed in various photoelectron and photo-ion yields. The left part of the table contains lifetimes of transients in ATI bands of various orders with photoelectron energies given by eqn (1). The right part shows ion yields of parent FLU ions ($C_{13}H_{10}^+$, $C_{13}H_{10}^{2+}$, $C_{13}H_{10}^{3+}$) and the monodehydrogenated FLU monocation ($C_{13}H_9^+$). The uncertainties of the lifetimes are the 1σ values obtained from the Monte-Carlo sampling

| ATI band order k	Lifetime, fs	Parent species	Lifetime, fs
1	102 ± 4	$C_{13}H_{10}^+$	62 ± 1
2	93 ± 3	$C_{13}H_9^+$	91 ± 1
3	87 ± 3	$C_{13}H_{10}^{2+}$	79 ± 1
4	90 ± 5	$C_{13}H_{10}^{3+}$	42 ± 6
5	83 ± 3		

In general, the strong-field induced dynamics are in many aspects similar to the dynamics observed by the XUV pulses.[13–19] This is direct evidence of general photochemical properties of the PAHs, dictated by their molecular and electronic structures, such as the closely connected carbon framework and a highly conjugated nature of π-bonds. However, there are some noticeable differences with the XUV regime, which are signs of the strong-field excitation character. Here, we will focus the discussion on the channels that were not observed with XUV excitation.

First, let us discuss the dynamics of the parent ions, given in Table 1. Unlike before, with the IR pump, we see short-lived transients in the monocations, corresponding to the lifetime of excited neutral FLU. We observed the transient peaks in both the intact parent FLU monocation ($C_{13}H_{10}^+$) and in its monodehydrogenated version ($C_{13}H_9^+$). The lifetime extracted from the $C_{13}H_9^+$ ion yield is 30 fs longer than the lifetime from $C_{13}H_{10}^+$, which is most likely a sign of the unresolved delay for the loss of hydrogen. The lifetime of the near-threshold FLU$^+$ observed in the yield of the parent dication $C_{13}H_{10}^{2+}$ is longer than for the excited neutral. This could be due to a larger density of the excited states with the increase of the charge state. The fitted lifetimes of the near-ionization-threshold FLU dication FLU^{2+}, observed through the pump–probe dependent IY of $C_{13}H_{10}^{3+}$, revealed a significantly shortened lifetime (42 ± 6 fs), compared to those obtained with the XUV pump (126 ± 16 fs in the XUV-IR experiment and 184 ± 44 fs in XUV-VIS).[19] This drastic difference probably arises from a difference in the distribution of the population of the FLU^{2+} excited states obtained in the strong-field and single-XUV-photon ionization regimes.

In the kinetic-energy resolved IY of the monocationic fragments (Fig. 7c and "Peak 1" in Fig. 10), we see the same channels as in the XUV experiments,[17,19] namely $(1,0) \rightarrow (1,1)$ and $(1,1) \rightarrow (2,1)$ (Fig. 8 and ESI†). However, because the low-energy IR pump photons do not necessarily ionize the molecule, a new channel was observed, namely $(0,0) \rightarrow (1,0)$, similar to that in the parent monocations (see Fig. 8). This channel has a much shorter lifetime on the order of a few fs to 10 fs than the analogous process in the parent ions (FLU$^0 \rightarrow$ FLU$^+$) with a lifetime of 62 ± 1 fs (see Table 1 and Fig. 9). Similar to the FLU$^0 \rightarrow$ FLU$^+$ and FLU$^+ \rightarrow$ FLU^{2+} channels (Table 1), we see
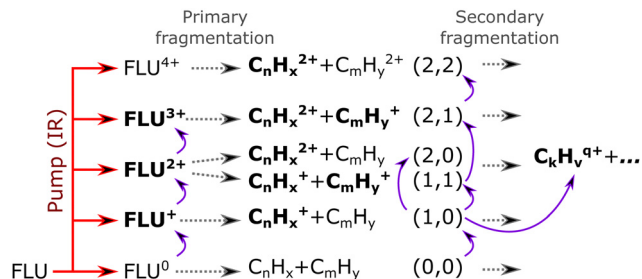

Fig. 8 Reaction scheme of the observed pump–probe dynamics in FLU under the influence of an intense IR pump pulse (indicated by a red arrow) and probed with a VIS pulse (indicated as curved violet arrows). The gray dashed arrows indicate possible evolution pathways of the excited-ionized ensemble of molecules. Species in bold font were observed in the experiment, whilst the normal font indicates unobserved or uncharged (and thus invisible in the MS) species.
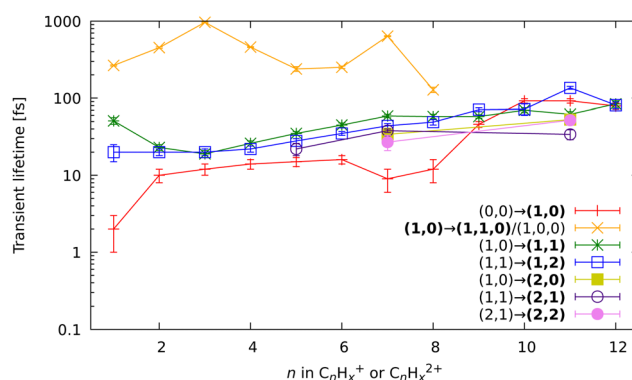
Fig. 9 All fitted relaxation lifetimes of the different fragmentation-related processes, extracted through the global fitting of the pump–probe dependent observables. The x-axis indicates the size of the fragment in which the corresponding lifetime was observed, and the y-axis shows lifetimes on a logarithmic scale. The bold font in the legend indicates in which channel of the fragment ion the transient was observed. The $(1,\ldots)$ and $(2,\ldots)$ bold channels' notation indicates that the lifetime was observed either in the monocationic or dicationic fragment, respectively.

shorter lifetimes of metastable species in $(0,0) \rightarrow (1,0)$ channels compared to $(1,0) \rightarrow (1,1)$ channels (Fig. 9). This trend can be again explained by the decreased density of states in the neutral metastable species with respect to their monocationic analogs. The additional decrease in lifetimes of $(0,0) \rightarrow (1,0)$ compared to the parent species (FLU$^0 \rightarrow$ FLU$^+$ channel) can be explained in the same fashion: the smaller the molecular species, the smaller the near-ionization threshold density of states.

Another previously unseen channel corresponds to slow dynamics with lifetimes of 0.1–1 ps observed in the $(1,0)$ channels of small ions (CH_x^+ to $C_8H_x^+$). An example of such a channel can be seen in Fig. 10, denoted as "Peak 2". This dynamic feature is a transient decrease for the fragments from $C_2H_x^+$ to $C_8H_x^+$, but for the CH_x^+, it is a transient increase. Therefore, we attribute this channel to the secondary dissociation of the larger ions, eventually ending up with the smallest CH_x^+ fragment. We can denote this channel as $(1,0) \rightarrow (1,1,0)/(1,0,0)$ (Fig. 9), meaning that after probing, three fragments are
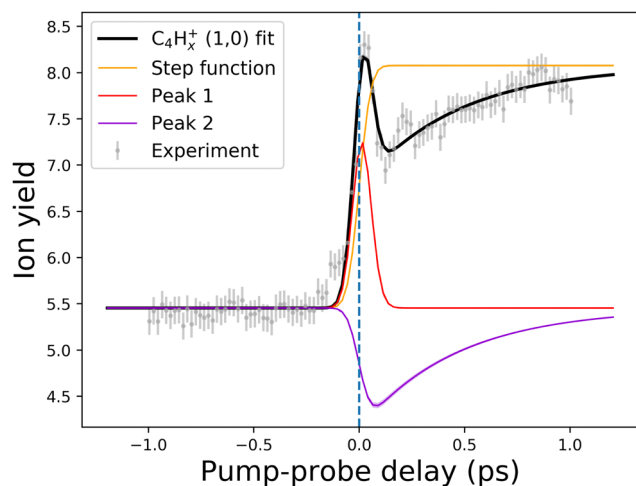
Fig. 10 An example of the pump–probe fit for the (1,0) channel of the $C_4H_x^+$ fragment. Points with error bars present experimental points retrieved from the PImMS camera, while the solid lines demonstrate the fitted curve (black line) and fit components (colored lines). The step function (yellow line) represents the static change in given ionic species production in the pump before probe and probe before pump regimes. Peak 1 (red line) corresponds to the (0,0) → (1,0) channel, while Peak 2 (violet line) corresponds to the (1,0) → (1,1,0)/(1,0,0) channel (see Fig. 8 and 9). The vertical dashed line shows the temporal overlap of pump and probe pulses. All the fits are available in the ESI.†

produced, either two monocations and one neutral, or one monocation and two neutrals. The slow transient lifetimes could be attributed to the relaxation lifetimes of the vibrationally and vibronically excited fragment ions that eventually fragment further upon the interaction with the probe pulse, leading to transient decay of its own ion yield and corresponding transient increase in the ion yield of the CH_x^+ species. Such fragmentation is consistent with observations from the static recoil-frame covariance analysis, which demonstrates secondary fragmentation patterns (see Section 3.2.3).

The last new set of channels that have not been observed before for FLU in the XUV-pump regime[19] are the (2,1) and (2,2) channels of the dicationic fragments ($C_7H_x^{2+}$, and $C_{11}H_x^{2+}$), as shown in Fig. 5. These channels indicate the lifetimes of the excited FLU trication (FLU^{3+}) and tetracation (FLU^{4+}). The lifetimes of these channels have similar values and show similar trends, as those observed in monocationic fragments for the (1,0) → (1,1) and (1,1) → (1,2) channels (Fig. 9). This might indicate that all these fragments are formed through a set of similar excited states of the di- and trications.

4 Conclusions

We investigated the behavior of fluorene ($C_{13}H_{10}$), a three-ring polycyclic aromatic hydrocarbon, under the influence of strong-field laser pulses and provided a complete disentanglement and characterization of the photochemical dynamics of fluorene in these photochemical conditions. Excitation by intense IR pulses tends to induce more secondary fragmentation and double and triple ionization than single-photon XUV

ionization, which is seen from the recoil-frame covariance analysis and pump–probe dynamics. The strong-field excitation also opens new channels that were not observed in the XUV ionization. First of all, this is the dynamics of the near-threshold neutral molecule, which produces previously unobserved features appearing from the presence of the excited neutral molecule. The second new observation is the tetracation formation, which was observed *via* the (2,2) channel of the dicationic fragments $C_7H_x^{2+}$ and $C_{11}H_x^{2+}$.

All the observed time-dependent channels in photoion and photoelectron spectra were included in a global fit. This fitting dataset consisted of four parent ions extracted from the mass spectra, 15 kinetic-energy resolved ionic fragments extracted from ion-velocity-map imaging, and five photoelectron channels obtained from electron-velocity-map imaging. From this analysis, we extracted 60 transient lifetimes corresponding to different photoinduced intermediates. This extensive dataset of the transient species' lifetimes of a prototypical polycyclic aromatic hydrocarbon provides new insights into the rich photochemistry of PAHs under the influence of intense electric fields.

Author contributions

Data availability

ESI† consists of (1) a PDF file with the fitting results and detailed complementary pictures to those presented in the manuscript, (2) a ZIP archive with the pre-processed experimental and theoretical data (including data analysis and plotting scripts) that can be used to reproduce the results and figures in the paper. All additional data is available by request from the corresponding author.

Conflicts of interest

There are no conflicts to declare.

Acknowledgements

This journal is © the Owner Societies 2024

Phys. Chem. Chem. Phys., 2024, **26**, 20261–20272 | **20269**

References

1 C. Joblin and A. Tielens, *EAS Publ. Ser.*, 2011, **46**, 3–10.

2 G. Lagache, H. Dole, J.-L. Puget, P. Pérez-González, E. Le Floch, G. H. Rieke, C. Papovich, E. Egami, A. Alonso-Herrero and C. Engelbracht, *et al.*, *Astrophys. J., Suppl. Ser.*, 2004, **154**, 112.

3 K. Srogi, *Environ. Chem. Lett.*, 2007, **5**, 169–195.

4 M. Låg, J. Øvrevik, M. Refsnes and J. A. Holme, *Respir. Res.*, 2020, **21**, 299.

5 H. Kaneda, T. Onaka, I. Sakon, D. Ishihara, A. Mouri, M. Yamagishi and A. Yasuda, *PAH Evolution in the Harsh Environment of the ISMSciences, Les Ulis*, 2011, pp. 157–168.

6 V. M. Bierbaum, V. L. Page and T. P. Snow, *PAHs and the Chemistry of the ISM, EDP Sciences, Les Ulis*, 2011, 427–440.

7 E. R. Micelotta, A. P. Jones and A. G. G. M. Tielens, *Astron. Astrophys.*, 2011, **526**, A52.

8 E. C. Sittler, J. F. Cooper, S. J. Sturner and A. Ali, *Icarus*, 2020, **344**, 113246.

9 T. Yatsuhashi and N. Nakashima, *J. Phys. Chem. A*, 2010, **114**, 7445–7452.

10 T. Yatsuhashi and N. Nakashima, *J. Phys. Chem. A*, 2005, **109**, 9414–9418.

11 L. Robson, K. Ledingham, A. Tasker, P. McKenna, T. McCanny, C. Kosmidis, D. Jaroszynski, D. Jones, R. Issac and S. Jamieson, *Chem. Phys. Lett.*, 2002, **360**, 382–389.

12 L. Robson, A. Tasker, K. Ledingham, P. McKenna, T. McCanny, C. Kosmidis, P. Tzallas, D. Jaroszynski and D. Jones, *Int. J. Mass Spectrom.*, 2002, **220**, 69–85.

13 A. Marciniak, V. Despré, T. Barillot, A. Rouzée, M. C. E. Galbraith, J. Klei, C.-H. Yang, C. T. L. Smeenk, V. Loriot, S. N. Reddy, A. G. G. M. Tielens, S. Mahapatra, A. I. Kuleff, M. J. J. Vrakking and F. Lépine, *Nat. Commun.*, 2015, **6**, 7909.

14 A. Marciniak, V. Despré, V. Loriot, G. Karras, M. Hervé, L. Quintard, F. Catoire, C. Joblin, E. Constant, A. I. Kuleff and F. Lépine, *Nat. Commun.*, 2019, **10**, 337.

15 M. Hervé, V. Despré, P. Castellanos Nash, V. Loriot, A. Boyer, A. Scognamiglio, G. Karras, R. Brédy, E. Constant, A. G. G. M. Tielens, A. I. Kuleff and F. Lépine, *Nat. Phys.*, 2021, **17**, 327–331.

16 A. Boyer, M. Hervé, V. Despré, P. Castellanos Nash, V. Loriot, A. Marciniak, A. G. G. M. Tielens, A. I. Kuleff and F. Lépine, *Phys. Rev. X*, 2021, **11**, 041012.

17 J. W. L. Lee, D. S. Tikhonov, P. Chopra, S. Maclot, A. L. Steber, S. Gruet, F. Allum, R. Boll, X. Cheng, S. Düsterer, B. Erk, D. Garg, L. He, D. Heathcote, M. Johny, M. M. Kazemi, H. Köckert, J. Lahl, A. K. Lemmens, D. Loru, R. Mason, E. Müller, T. Mullins, P. Olshin, C. Passow, J. Peschel, D. Ramm, D. Rompotis, N. Schirmel, S. Trippel, J. Wiese, F. Ziaee, S. Bari, M. Burt, J. Küpper, A. M. Rijs, D. Rolles, S. Techert, P. Eng-Johnsson, M. Brouard, C. Vallance, B. Manschwetus and M. Schnell, *Nat. Commun.*, 2021, **12**, 6107.

18 J. W. L. Lee, D. S. Tikhonov, F. Allum, R. Boll, P. Chopra, B. Erk, S. Gruet, L. He, D. Heathcote, M. M. Kazemi, J. Lahl, A. K. Lemmens, D. Loru, S. Maclot, R. Mason, E. Müller, T. Mullins, C. Passow, J. Peschel, D. Ramm, A. L. Steber, S. Bari, M. Brouard, M. Burt, J. Küpper, P. Eng-Johnsson, A. M. Rijs, D. Rolles, C. Vallance, B. Manschwetus and M. Schnell, *Phys. Chem. Chem. Phys.*, 2022, **24**, 23096–23105.

19 D. Garg, J. W. L. Lee, D. S. Tikhonov, P. Chopra, A. L. Steber, A. K. Lemmens, B. Erk, F. Allum, R. Boll, X. Cheng, S. Düsterer, S. Gruet, L. He, D. Heathcote, M. Johny, M. M. Kazemi, H. Köckert, J. Lahl, D. Loru, S. Maclot, R. Mason, E. Müller, T. Mullins, P. Olshin, C. Passow, J. Peschel, D. Ramm, D. Rompotis, S. Trippel, J. Wiese, F. Ziaee, S. Bari, M. Burt, J. Küpper, A. M. Rijs, D. Rolles, S. Techert, P. Eng-Johnsson, M. Brouard, C. Vallance, B. Manschwetus and M. Schnell, *Front. Phys.*, 2022, **10**, 880793.

20 L. Zhou, Y. Liu, T. Sun, S. Feng, H. Lv and H. Xu, *J. Phys. Chem. A*, 2019, **123**, 8365–8369.

21 L. Zhou, Y. Liu, T. Sun, H. Yin, Y. Zhao, H. Lv and H. Xu, *J. Phys. Chem. A*, 2021, **125**, 2095–2100.

22 M. L. Vidal, M. Epshtein, V. Scutelnic, Z. Yang, T. Xue, S. R. Leone, A. I. Krylov and S. Coriani, *J. Phys. Chem. A*, 2020, **124**, 9532–9541.

23 M. Epshtein, V. Scutelnic, Z. Yang, T. Xue, M. L. Vidal, A. I. Krylov, S. Coriani and S. R. Leone, *J. Phys. Chem. A*, 2020, **124**, 9524–9531.

20270 | *Phys. Chem. Chem. Phys.*, 2024, **26**, 20261–20272

This journal is © the Owner Societies 2024

24 A. M. Burkhardt, K. L. K. Lee, P. B. Changala, C. N. Shingledecker, I. R. Cooke, R. A. Loomis, H. Wei, S. B. Charnley, E. Herbst, M. C. McCarthy and B. A. McGuire, *Astrophys. J. Lett.*, 2021, **913**, L18.

25 J. Cernicharo, M. Agúndez, C. Cabezas, B. Tercero, N. Marcelino, J. R. Pardo and P. de Vicente, *Astron. Astrophys.*, 2021, **649**, L15.

26 L. Keldysh, *J. Exp. Theor. Phys.*, 1965, **20**, 1307–1314.

27 B. Erk, J. P. Müller, C. Bomme, R. Boll, G. Brenner, H. N. Chapman, J. Correa, S. Düsterer, S. Dziarzhytski, S. Eisebitt, H. Graafsma, S. Grunewald, L. Gumprecht, R. Hartmann, G. Hauser, B. Keitel, C. von Korff Schmising, M. Kuhlmann, B. Manschwetus, L. Mercadier, E. Müller, C. Passow, E. Plönjes, D. Ramm, D. Rompotis, A. Rudenko, D. Rupp, M. Sauppe, F. Siewert, D. Schlosser, L. Strüder, A. Swiderski, S. Techert, K. Tiedtke, T. Tilp, R. Treusch, I. Schlichting, J. Ullrich, R. Moshammer, T. Möller and D. Rolles, *J. Synchrotron Radiat.*, 2018, **25**, 1529–1540.

28 J. Feldhaus, *J. Phys. B: At., Mol. Opt. Phys.*, 2010, **43**, 194002.

29 H. Redlin, A. Al-Shemmary, A. Azima, N. Stojanovic, F. Tavella, I. Will and S. Düsterer, *Nuclear Instruments and Methods in Physics Research Section A: Accelerators, Spectrometers, Detectors and Associated Equipment*, 2011, **635**, S88–S93.

30 P. Chopra, PhD thesis, Christian-Albrechts-Universität zu Kiel, Germany, 2022.

31 A. T. Eppink and D. H. Parker, *Rev. Sci. Instrum.*, 1997, **68**, 3477–3484.

32 D. H. Parker and A. T. Eppink, *J. Chem. Phys.*, 1997, **107**, 2357–2362.

33 U. Even, *EPJ Tech. Instrum.*, 2015, **2**, 17.

34 A. T. Clark, J. P. Crooks, I. Sedgwick, R. Turchetta, J. W. L. Lee, J. J. John, E. S. Wilman, L. Hill, E. Halford, C. S. Slater, B. Winter, W. H. Yuen, S. H. Gardiner, M. L. Lipciuc, M. Brouard, A. Nomerotski and C. Vallance, *J. Phys. Chem. A*, 2012, **116**, 10897–10903.

35 K. Amini, S. Blake, M. Brouard, M. B. Burt, E. Halford, A. Lauer, C. S. Slater, J. W. L. Lee and C. Vallance, *Rev. Sci. Instrum.*, 2015, **86**, 103113.

36 A. L. Steber and E. Müller, *Beamtime DAQ Access*, 2021, **https://stash.desy.de/projects/CS/repos/pah/browse**.

37 D. S. Tikhonov, D. Garg and P. Chopra, *CAMPFancyAnalysis*, 2023, **https://gitlab.desy.de/denis.tikhonov/campfancyanalysis**.

38 C. Bordas, F. Paulig, H. Helm and D. L. Huestis, *Rev. Sci. Instrum.*, 1996, **67**, 2257–2268.

39 S. Gibson, D. D. Hickstein, R. Yurchak, M. Ryazanov, D. Das and G. Shih, *PyAbel/PyAbel: v0.9.0*, 2022, DOI: **10.5281/zenodo.7438595**.

40 D. D. Hickstein, S. T. Gibson, R. Yurchak, D. D. Das and M. Ryazanov, *Rev. Sci. Instrum.*, 2019, **90**, 065115.

41 L. Minion, J. W. L. Lee and M. Burt, *Phys. Chem. Chem. Phys.*, 2022, **24**, 11636–11645.

42 C. S. Slater, S. Blake, M. Brouard, A. Lauer, C. Vallance, J. J. John, R. Turchetta, A. Nomerotski, L. Christensen and J. H. Nielsen, *et al.*, *Phys. Rev. A*, 2014, **89**, 011401.

43 C. S. Slater, S. Blake, M. Brouard, A. Lauer, C. Vallance, C. S. Bohun, L. Christensen, J. H. Nielsen, M. P. Johansson and H. Stapelfeldt, *Phys. Rev. A*, 2015, **91**, 053424.

44 F. Allum, M. Burt, K. Amini, R. Boll, H. Köckert, P. K. Olshin, S. Bari, C. Bomme, F. Brauße and B. Cunha de Miranda, *et al.*, *J. Chem. Phys.*, 2018, **149**, 204313.

45 K. Amini, R. Boll, A. Lauer, M. Burt, J. W. Lee, L. Christensen, F. Brauße, T. Mullins, E. Savelyev and U. Ablikim, *et al.*, *J. Chem. Phys.*, 2017, **147**, 013933.

46 J. Mikosch and S. Patchkovskii, *J. Mod. Opt.*, 2013, **60**, 1426–1438.

47 F. Allum, V. Music, L. Inhester, R. Boll, B. Erk, P. Schmidt, T. M. Baumann, G. Brenner, M. Burt, P. V. Demekhin, S. Dörner, A. Ehresmann, A. Galler, P. Grychtol, D. Heathcote, D. Kargin, M. Larsson, J. W. L. Lee, Z. Li, B. Manschwetus, L. Marder, R. Mason, M. Meyer, H. Otto, C. Passow, R. Pietschnig, D. Ramm, K. Schubert, L. Schwob, R. D. Thomas, C. Vallance, I. Vidanović, C. von Korff Schmising, R. Wagner, P. Walter, V. Zhaunerchyk, D. Rolles, S. Bari, M. Brouard and M. Ilchen, *Commun. Chem.*, 2022, **5**, 42.

48 L. J. Frasinski, *J. Phys. B: At., Mol. Opt. Phys.*, 2016, **49**, 152004.

49 S. Pedersen and A. Zewail, *Mol. Phys.*, 1996, **89**, 1455–1502.

50 D. S. Tikhonov, D. Garg and M. Schnell, *Photochemistry*, 2024, **4**, 57–110.

51 D. S. Tikhonov, MC^3 Fitting, 2021, **https://gitlab.desy.de/denis.tikhonov/mcmcmcfitting**.

52 D. S. Tikhonov, PyRAMD, 2023, **https://gitlab.desy.de/denis.tikhonov/pyramd**.

53 S. Grimme, *Angew. Chem., Int. Ed.*, 2013, **52**, 6306–6312.

54 C. A. Bauer and S. Grimme, *J. Phys. Chem. A*, 2016, **120**, 3755–3766.

55 D. S. Tikhonov, A. Datta, P. Chopra, A. L. Steber, B. Manschwetus and M. Schnell, *Z. Phys. Chem.*, 2020, **234**, 1507–1531.

56 C. Bannwarth, E. Caldeweyher, S. Ehlert, A. Hansen, P. Pracht, J. Seibert, S. Spicher and S. Grimme, *WIREs Comput. Mol. Sci.*, 2021, **11**, e1493.

57 C. Bannwarth, S. Ehlert and S. Grimme, *J. Chem. Theory Comput.*, 2019, **15**, 1652–1671.

58 J. Koopman and S. Grimme, *ACS Omega*, 2019, **4**, 15120–15133.

59 J. Cížek, *J. Chem. Phys.*, 1966, **45**, 4256–4266.

60 T. H. Dunning, *J. Chemical Phys.*, 1989, **90**, 1007–1023.

61 R. A. Kendall, T. H. Dunning and R. J. Harrison, *J. Chem. Phys.*, 1992, **96**, 6796–6806.

62 F. Neese, F. Wennmohs, U. Becker and C. Riplinger, *J. Chem. Phys.*, 2020, **152**, 224108.

63 J.-F. Zhang, H. Lü, W.-L. Zuo, H.-F. Xu, M.-X. Jin and D.-J. Ding, *Chin. Phys. B*, 2015, **24**, 113301.

64 A. Kitashoji, A. Fujihara, T. Yoshikawa and T. Yatsuhashi, *Chem. Lett.*, 2019, **48**, 1472–1475.

65 T. Kawaguchi, K. Kitagawa, K. Toyota, M. Kozaki, K. Okada, N. Nakashima and T. Yatsuhashi, *J. Phys. Chem. A*, 2021, **125**, 8014–8024.

66 W. A. Bryan, S. L. Stebbings, J. McKenna, E. M. L. English, M. Suresh, J. Wood, B. Srigengan, I. C. E. Turcu, J. M. Smith,

This journal is © the Owner Societies 2024

Phys. Chem. Chem. Phys., 2024, **26**, 20261–20272 | **20271**

E. J. Divall, C. J. Hooker, A. J. Langley, J. L. Collier, I. D. Williams and W. R. Newell, *Nat. Phys.*, 2006, **2**, 379–383.

67 M. G. Pullen, B. Wolter, X. Wang, X.-M. Tong, M. Sclafani, M. Baudisch, H. Pires, C. D. Schröter, J. Ullrich, T. Pfeifer, R. Moshammer, J. H. Eberly and J. Biegert, *Phys. Rev. A*, 2017, **96**, 033401.

68 J. H. Eberly and J. Javanainen, *Eur. J. Phys.*, 1988, **9**, 265.

69 R. R. Freeman, P. H. Bucksbaum, H. Milchberg, S. Darack, D. Schumacher and M. E. Geusic, *Phys. Rev. Lett.*, 1987, **59**, 1092–1095.

70 K. Lin, S. Eckart, A. Hartung, D. Trabert, K. Fehre, J. Rist, L. P. H. Schmidt, M. S. Schöffler, T. Jahnke, M. Kunitski and R. Dörner, *Sci. Adv.*, 2022, **8**, eabn7386.

71 R. Wang, Q. Zhang, D. Li, S. Xu, P. Cao, Y. Zhou, W. Cao and P. Lu, *Opt. Express*, 2019, **27**, 6471–6482.

72 M. Frenklach and H. Wang, *Symp. (Int.) Combust.*, 1991, **23**, 1559–1566.

73 V. V. Kislov, N. I. Islamova, A. M. Kolker, S. H. Lin and A. M. Mebel, *J. Chem. Theory Comput.*, 2005, **1**, 908–924.

74 D. S. N. Parker, R. I. Kaiser, T. P. Troy and M. Ahmed, *Angew. Chem., Int. Ed.*, 2014, **53**, 7740–7744.

75 K. Miyamoto, S. Narita, Y. Masumoto, T. Hashishin, T. Osawa, M. Kimura, M. Ochiai and M. Uchiyama, *Nat. Commun.*, 2020, **11**, 2134.

76 H. W. Lin, C.-H. Lee, D. W. Gerdes, F. C. Adams, J. Becker, K. Napier and L. Markwardt, *Astrophysical J. Lett.*, 2020, **889**, L30.

20272 | *Phys. Chem. Chem. Phys.*, 2024, **26**, 20261–20272

This journal is © the Owner Societies 2024